

This is an Open Access document downloaded from ORCA, Cardiff University's institutional repository: <https://orca.cardiff.ac.uk/id/eprint/126620/>

This is the author's version of a work that was submitted to / accepted for publication.

Citation for final published version:

Smith, Gemma L., Eyley, Jennifer E., Han, Xue, Zhang, Xinran, Li, Jiangnan, Jacques, Nicholas M., Godfrey, Harry G. W., Argent, Stephen P., McCormick McPherson, Laura J., Teat, Simon J., Cheng, Yongqiang, Frogley, Mark D., Cinque, Gianfelice, Day, Sarah J., Tang, Chiu C., Easun, Timothy L., Rudic, Svemir, Ramirez-Cuesta, Anibal J., Yang, Sihai and Schröder, Martin 2019. Reversible coordinative binding and separation of sulfur dioxide in a robust metal-organic framework with open copper sites. *Nature Materials* 18, pp. 1358-1365. 10.1038/s41563-019-0495-0

Publishers page: <http://dx.doi.org/10.1038/s41563-019-0495-0>

Please note:

Changes made as a result of publishing processes such as copy-editing, formatting and page numbers may not be reflected in this version. For the definitive version of this publication, please refer to the published source. You are advised to consult the publisher's version if you wish to cite this paper.

This version is being made available in accordance with publisher policies. See <http://orca.cf.ac.uk/policies.html> for usage policies. Copyright and moral rights for publications made available in ORCA are retained by the copyright holders.



Reversible coordinative binding and separation of sulphur dioxide in a robust metal-organic framework with open copper sites

Gemma L. Smith,^{1,a} Jennifer E. Eyley,^{1,a} Xue Han,¹ Xinran Zhang¹, Jiangnan Li,¹ Nicholas M. Jacques,¹ Harry G.W. Godfrey,¹ Stephen P. Argent,² Laura J. McCormick,³ Simon J. Teat,³ Yongqiang Cheng,⁴ Mark D. Frogley,⁵ Gianfelice Cinque,⁵ Sarah J. Day,⁵ Chiu C. Tang,⁵ Timothy L. Easun,⁶ Svemir Rudić,⁷ Anibal J. Ramirez-Cuesta,⁴ Sihai Yang^{1*} and Martin Schröder^{1*}

1. School of Chemistry, University of Manchester, Manchester, M13 9PL (UK)

2. Department of Chemistry, University of Warwick, CV4 7AL (UK)

3. Advanced Light Source, Lawrence Berkeley National Laboratory, Berkeley, California 94720 (USA)

4. Oak Ridge National Laboratory, Oak Ridge, TN 37831(USA)

5. Diamond Light Source, Harwell Science Campus, Oxfordshire, OX11 0DE (UK)

6. School of Chemistry, Cardiff University, Cardiff, CF10 3AT (UK)

7. ISIS Facility, STFC Rutherford Appleton Laboratory, Chilton, Oxfordshire, OX11 0QX (UK)

a. these authors contributed equally to this work.

Emissions of sulphur dioxide (SO₂) from flue gas and marine transport have detrimental impacts on the environment and human health, but SO₂ is also an important industry feedstock if it can be recovered, stored and transported efficiently. Here we report the exceptional adsorption and separation of SO₂ in a new porous material, [Cu₂(L)] (H₄L = 4',4'''-(pyridine-3,5-diyl)bis([1,1'-biphenyl]-3,5-dicarboxylic acid), MFM-170. MFM-170 exhibits fully reversible SO₂ uptake of 17.5 mmol g⁻¹ at 298 K, 1.0 bar, and the SO₂ binding domains for trapped molecules within MFM-170 have been determined. Significantly, we report the first example of reversible co-ordination of SO₂ to open Cu(II) sites in a porous material, contributing to excellent adsorption thermodynamics and selectivities for SO₂ binding, as well as facile regeneration of MFM-170 post adsorption. MFM-170 is stable to water, acid and base and shows significant promise for the dynamic separation of SO₂ from simulated flue gas mixtures, as confirmed by breakthrough experiments.

The use of fossil fuels is a major contributor to many serious environmental issues, but transition to clean energy sources remains challenging as new technologies take time to fully develop. A significant problem is the release of SO₂, for which anthropogenic sources account for >87% of global emissions.¹ SO₂ has detrimental effects on the environment and human health, but is also an important feedstock for the production of sulphuric acid. Furthermore, trace amounts of SO₂ can greatly reduce the activity of amine-based scrubbers for CO₂ from flue gas,² as well as irreversibly poisoning catalysts for selective NO_x reduction³ and CH₄ combustion.⁴

In recent years, there has been growing interest in the development of dry regenerable sorbents for SO₂ operating under ambient conditions.⁵⁻⁷ These materials offer advantages over existing wet flue gas desulphurisation (FDG) technologies by reducing energy and water requirements and minimising the generation of solid and liquid waste. Importantly, regeneration of sorbents allows recovery of saleable SO₂, which can be utilised further *via* conversion to elemental sulphur or sulfuric acid. Regenerable SO₂ sorbents are often used for scrubbing of sulphur by absorption of acid plant tail gases, as well as smelter off-gases (containing up to 8% SO₂), allowing the recovered SO₂ to be cycled to the front end of the plant.⁸ These processes are typically based on alkaline solutions, which require high temperatures and/or further reaction for regeneration. Desirable properties of solid sorbents operating *via* pressure swing adsorption (PSA) mechanisms include: (i) high SO₂ capacity, (ii) rapid sorption rate, (iii) low attrition rate (no loss of SO₂ capacity over many cycles), (iv) ease of regeneration, and (v) high selectivity. High capacity sorbents for SO₂ can also be used for safe transportation of recovered gaseous SO₂ under ambient conditions, without the large energy demands required for pressurisation to liquid SO₂ or reduction to solid elemental sulphur.

Porous metal-organic frameworks (MOFs) are emerging sorbents that have been studied extensively for uptake and separation of a wide variety of gases, notably CO₂, H₂ and hydrocarbons,⁹⁻¹⁴ but their application to SO₂ capture has been hindered by the toxic and highly corrosive nature of this substrate. To date, several MOFs have been tested as SO₂ adsorbents (Table 1, Fig 2),¹⁵⁻²⁵ but many exhibit limited stability and/or reversibility under near-ambient conditions. Current top-performing MOFs for SO₂

adsorption at 298 K and 1.0 bar include MFM-202a (10.2 mmol g^{-1})¹⁸ and SIFSIX-1-Cu (11.0 mmol g^{-1})¹⁶. The former is subject to an irreversible phase change on SO₂ uptake, whilst the steep uptake of the latter may render it unfeasible for practical PSA applications.^{26,27} Indeed, a trade-off often exists between the uptake at low-pressure and the energy cost of system regeneration. Another consideration is that sorbents for use in FGD processes must be located upstream of CO₂ scrubbing units, and therefore require high selectivity for SO₂ over CO₂ at low partial pressures of SO₂ (~2000 ppm). Although open metal sites in MOFs can improve gas binding selectivity, the resultant MOFs are often subject to severe framework degradation upon contact with water, precluding their practical applications.²⁸⁻³¹ Similarly, coordination of strongly complexing SO₂ molecules to open metal centres can disrupt the linker-metal coordination and cause structural collapse.

Herein, we report the first example of reversible coordinative binding of SO₂ to open Cu(II) sites in a remarkably robust material, MFM-170, leading to optimal adsorption and selectivity for SO₂. Coordination of the pyridyl N-donor to one axial site of the Cu₂(O₂CR)₄ paddlewheel unit leads to an unusual (3,36)-connected *txt* framework which, on removal of axial water, affords one open Cu(II) site per Cu₂(O₂CR)₄ paddlewheel in MFM-170. Significantly, at 298 K and 1.0 bar, MFM-170 exhibits an unprecedented uptake of SO₂ of 17.5 mmol g^{-1} , which can be fully regenerated at ambient temperature. We have unravelled the high selectivity of MFM-170 for SO₂ and have probed the nature of host-guest binding using *in situ* single crystal X-ray diffraction, FTIR micro-spectroscopy and neutron scattering. Importantly, breakthrough experiments of simulated flue gas mixtures demonstrate that MFM-170 has excellent separation properties, even in the presence of water and at elevated temperatures (up to 348 K). The stability of MFM-170 to wet SO₂ has been confirmed by long duration synchrotron X-ray diffraction experiments. Furthermore, we directly investigate the effect of the open copper sites on SO₂ uptake and selectivity by comparing MFM-170 to the coordinatively saturated parent structure MFM-170·H₂O, in which H₂O is retained at the axial Cu(II) site within the Cu₂(O₂CR)₄ paddlewheel.

Results and Discussions

Synthesis and structural analysis of MFM-170·solv. Solvothermal reaction of a pyridine-containing tetracarboxylate linker 4',4'''-(pyridine-3,5-diyl)bis([1,1'-biphenyl]-3,5-dicarboxylic acid) (H₄L, Fig. 1a) and Cu(NO₃)₂·2.5H₂O in a mixture of DMF and H₂O (v/v = 5:1) under acidic conditions (HNO₃) yielded blue octahedral crystals of [Cu₂(L)(H₂O)]·6DMF, denoted as MFM-170·H₂O·solv. Single crystal X-ray diffraction reveals that MFM-170·H₂O·solv crystallises in the cubic space group *Im-3m* to form a rarely observed (3,36)-connected net with *txt* topology (Fig. 1b).³²⁻³⁴ The metal cluster consists of a Cu₂(O₂CR)₄ paddlewheel with four isophthalate units occupying the equatorial sites and one pyridyl N-donor from the ligand coordinating to the axial site of one Cu atom. The axial position of the other Cu atom of the Cu₂(O₂CR)₄ unit is occupied by a water molecule. The framework is constructed from Cu₂₄(RC₆H₃(CO₂)₂)₂₄ cuboctahedron, which acts as a 36-connected node, joined in a cubic array to six adjacent cuboctahedra by four ligands each (Fig. 1c). The overall framework can be visualised as this smaller cubic net which is connected to a secondary identical net *via* the 12 corners of the cuboctahedra *via* Cu-N bonds (Fig. 1d).

Thus, each ligand is a 3-connected node, with two isophthalate moieties that each connect an edge of a cuboctahedron, and one pyridyl N atom which joins a corner of a cuboctahedron.

The interconnected void spaces in MFM-170 can be considered as three distinct cages, denoted as **A**, **B** and **C** (Fig. 1e). The metal-organic cuboctahedra (denoted as cage **A**) have a dimension of 15.9 Å, comprised of alternating triangular and square faces. Each square face of cage **A** joins it to a cage **B**, which is formed by four V-shaped linkers bowing outward to create a prolate pore (width of 16.3 Å; length of 22.2 Å). Cage **C** is the smallest of the three and connects the triangular faces of cage **A**, measuring 12.8 Å between opposite triangular faces, and 14.2 Å between opposite C atoms.

Thermal and chemical stability of MFM-170. Thermogravimetric analysis (TGA) of MFM-170·H₂O·solv shows thermal stability up to ~620 K, confirmed by variable temperature PXRD analysis (Figs. S4, S8). The chemical robustness of MFM-170·H₂O·solv was investigated by exposing an as-synthesised sample to a range of harsh environmental conditions, including suspending the sample in boiling water and aqueous solutions of pH between 2-12. No loss in crystallinity was observed by PXRD after exposure to these conditions (Figs. 4b, S2, S3, S6). More importantly, desolvated MFM-170 can be re-hydrated fully and reversibly to give MFM-170·H₂O upon contact with water without loss of crystallinity. Reversible water adsorption isotherms at 293 and 303 K are shown in Fig. S10. To assess the long-term stability of MFM-170 to humid SO₂ and water, synchrotron PXRD data were collected for wet SO₂-loaded MFM-170 samples every week for 10 weeks (Fig. S7; see SI for further details). No loss of crystallinity or change in the structure of this material was observed (Table S3), confirming the excellent chemical resilience of the framework. The remarkable stability of MFM-170 is attributed to the unusual framework connectivity where the axially-coordinated pyridyl N-donors interlock the two cubic nets and block one of the two axial Cu(II) sites.

Analysis of gas adsorption isotherms of MFM-170 and MFM-170·H₂O. Desolvated MFM-170 possesses a BET surface area of 2408 m² g⁻¹ (consistent with the calculated surface area of 2456 m² g⁻¹ based upon the crystal structure) and a pore volume of 0.88 cm³ g⁻¹ (calculated from the N₂ isotherm at 77 K, Fig. S9), consistent with that (0.87 cm³ g⁻¹; solvent-accessible void space of 61%) derived from the single crystal structure. Significantly, MFM-170 shows an unprecedented SO₂ uptake of 19.4 mmol g⁻¹ (or 1.24 g g⁻¹) at 273 K and 1.0 bar (Fig. 3). To the best of our knowledge, this represents the highest known SO₂ uptake capacity in porous materials, followed by MFM-601 (16.9 mmol g⁻¹)¹⁵, MFM-202a (13.0 mmol g⁻¹)¹⁸ and mesoporous silicate MCM-41 (11.6 mmol g⁻¹)³⁵ under the same conditions. The performance of state-of-the-art porous materials under ambient conditions is summarised in Table 1 and Fig. 2, where a general linear relationship between SO₂ uptake and BET surface area is observed. MFM-170 exhibits the highest reported SO₂ adsorption capacity of 17.5 mmol g⁻¹ at 298 K and 1.0 bar, notably exceeding the current leading MOFs, such as MFM-601 (12.3 mmol g⁻¹)¹⁵, SIFSIX-1-Cu (11.0 mmol g⁻¹)¹⁶, [Zn₂(L₁)₂(bipy)] (10.9 mmol g⁻¹, at 293 K),¹⁷ and Ni(bdc)(ted)_{0.5} (10.0 mmol g⁻¹).¹⁹ At 298 K and 1.0 bar, the volumetric storage density of SO₂ in MFM-170 is 307 times that of gaseous SO₂ under the same conditions, or 75 times of that of compressed SO₂ (P₀ = 3.9 bar) in a pressure vessel (packing efficiency and system volume are not taken into consideration). Furthermore, MFM-170 shows high SO₂ adsorption

at elevated temperatures (11.6 mmol g⁻¹ at 333 K and 1 bar). Uptake of SO₂ in MFM-170 shows a reversible type I isotherm with high uptakes at low pressure (Fig. 3); at 273 K the uptake at 0.03 bar is 6.5 mmol g⁻¹. Despite the high uptake at low pressure, the excellent reversibility of the SO₂ isotherms at 273-333 K indicates that MFM-170 can be fully regenerated under pressure-swing conditions. More significantly, no loss of adsorption capacity of SO₂ was detected in MFM-170 after 50 adsorption-desorption cycles at 298 K, and PXRD analysis of MFM-170 after these 50 cycles confirms the full retention of crystal structure, reflecting the exceptional chemical and thermal stability of this material (Fig. 4).

To probe the effect of the open metal sites on SO₂ uptake, isotherms were measured for the coordinatively saturated parent material, MFM-170·H₂O, in which the axial water molecule is retained on the Cu(II) site. The SO₂ isotherm of MFM-170·H₂O at 273 K shows a reduced but still exceptionally high uptake of SO₂ (16.2 mmol g⁻¹) (Fig. S15). The difference in adsorption at 1.0 bar between MFM-170·H₂O and MFM-170 corresponds to approximately twice the density of open Cu(II) sites (1.46 mmol g⁻¹), suggesting that the presence of open metal sites has a key role in promoting the SO₂ uptake.

In comparison to the high SO₂ uptake at 298 K and 1 bar, MFM-170 uptakes only 3.04 mmol g⁻¹ of CO₂, 1.33 mmol g⁻¹ of CH₄, 0.38 mmol g⁻¹ of CO and 0.28 mmol g⁻¹ of N₂ under the same conditions (Figs. 3a, S11-14). The selectivity values of MFM-170 for SO₂/CO₂, SO₂/N₂, SO₂/CO and SO₂/CH₄ were calculated from single component isotherms at 298 K (Figs. S19, S20). Due to the negligible interaction of N₂ with the framework, MFM-170 exhibits a high IAST selectivity of 944 for an equimolar mixture of SO₂/N₂ at 1.0 bar. Furthermore, MFM-170 also has high selectivity values of 260, 203 and 35 for SO₂/CH₄, SO₂/CO and SO₂/CO₂, respectively. More importantly and considering the relatively low concentrations of SO₂ present in flue gas, decreasing the SO₂:X ratio from 50:50 to 1:99 still affords high selectivity values for SO₂/N₂ (260) and SO₂/CO₂ (28). These values are lower than those reported for SIFSIX-2-Cu-i,¹⁶ which possesses much narrower pores than MFM-170.

Determination of the binding domains for adsorbed SO₂ molecules in MFM-170 and MFM-170·H₂O. The binding domains of SO₂ were studied using *in situ* synchrotron X-ray single crystal diffraction. Structural analysis of desolvated MFM-170 confirms the complete removal of free solvents in the pore and bound water molecules on the Cu(II) sites, generating twelve open Cu(II) sites on the internal surface of cage **A** in desolvated MFM-170. Refinement of the diffraction data for the SO₂-loaded sample at 298 K revealed significant residual electron densities which were sequentially assigned as six distinct binding sites (**1-6**) in order of decreasing occupancy, giving a formula of [Cu₂(L)(SO₂)_{0.67}](SO₂)_{4.79} (denoted as MFM-170·5.46SO₂) (Fig. 5). Interestingly, the smallest cage **C** accounts for ~45% of all located SO₂ molecules, whilst ~25% is found in the cuboctahedral cage **A**. No ordered SO₂ molecules were located in the largest cage **B** reflecting the large void space and lack of functional groups lining the pore.

The primary binding site, **1**, is situated on a three-fold rotational axis in the triangular window of cage **A** and has full occupancy. The S_{SO₂} atom points towards the Cu₂(O₂CR)₄ paddlewheel, forming close contacts with two carboxylate O centers [S_{SO₂}(δ⁺)⋯(δ⁻)O = 3.16(3) Å]. Simultaneously, the O_{SO₂} atom located in the centre of the window forms a three-fold supplementary interaction to the isophthalate C-H

groups lining the window [$O_{SO_2} \cdots C = 4.18(3) \text{ \AA}$, $\angle O \cdots H-C = 140.5(6)^\circ$]. $SO_2(2)$ is coordinated to the open Cu(II) site in an end-on manner [$O_{SO_2}-Cu = 2.28(10) \text{ \AA}$] with an occupancy of 0.67. The $O_{SO_2}-Cu$ bond distance is shorter than the sum of van der Waals radius of Cu and O (2.92 \AA), confirming the formation of a covalent bond. The two O_{SO_2} atoms are parallel to the $Cu \cdots Cu$ axis, whilst the S_{SO_2} is disordered about a C_2 axis. Significantly, this is the first crystallographic example of SO_2 coordination at open metal sites within a MOF structure. Remarkably, the Cu(II) center is not the most occupied site, which is at least in part due to steric hindrance created by site **1**; the twelve Cu(II) sites line the internal surface of cage **A** and are therefore accessed through the square faces as the triangular windows are fully occupied by SO_2 molecules.

$SO_2(3)$ (occupancy = 0.47) is located in a crevice between cage **B** of one net and a perpendicular cage **B** of the second net. This small pocket accommodates interactions with the face of the pyridine ring [$S_{SO_2} \cdots N = 3.48(18) \text{ \AA}$] and phenyl H atoms [$O_{SO_2} \cdots C^4 = 3.20(4) \text{ \AA}$, $O_{SO_2} \cdots C^{11} = 4.80(4) \text{ \AA}$], accounting for ~30% of all located SO_2 molecules. $SO_2(4)$ (occupancy = 0.32), is found in cage **C** and situated with the S atom facing the carboxylate oxygens of the paddlewheel [$S_{SO_2}(\delta^+) \cdots (\delta^-)O^1 = 3.67(3) \text{ \AA}$] and interacts with neighbouring phenyl rings [$O_{SO_2} \cdots C^7 = 3.70(5) \text{ \AA}$, $O_{SO_2} \cdots \text{ring centroid} = 3.26(5) \text{ \AA}$]. $SO_2(5)$ is found in the square face between cages **A** and **B** with an occupancy of 0.26. Whilst no significant interaction with the framework was identified, dipole interactions between the adsorbed SO_2 molecules were observed [$S_{SO_2(2)} \cdots O_{SO_2(5)} = 2.54(6) \text{ \AA}$, $O_{SO_2(5)} \cdots S_{SO_2(6)} = 2.88(5) \text{ \AA}$]. The least populated site (**6**) (occupancy = 0.23) is sandwiched between two phenyl rings in cage **C** and forms interactions between the $S(\delta^+)$ and the phenyl π -electrons at distances of $3.28(15)$ and $3.30(15) \text{ \AA}$, measured between the ring centroids and S_{SO_2} .

We sought to examine the most thermodynamically favoured site *via* controlled desorption of MFM-170·5.46 SO_2 . Crucially, diffraction data collected for the sample under dynamic vacuum at 298 K showed that almost all adsorbed SO_2 molecules were removed from the structure of MFM-170, leaving just the Cu(II)-bound $SO_2(2)$ with an occupancy of 0.09. This confirms that the Cu(II) site is indeed the thermodynamically strongest binding site but is sufficiently weak to be almost entirely desorbed on reduction of pressure. Interestingly, DFT calculations indicated that for MOF-74(M) (M = Mg, Ni, Co, Zn), the sites with highest binding energies for SO_2 were located at the open metal sites.³⁷ For MFM-170 the multi-site cooperative binding between SO_2 molecules results in an optimal balance of high selectivity and excellent reversibility of the SO_2 adsorption that is observed. Subsequent brief heating to 400 K fully regenerated MFM-170 without any loss of crystallinity.

To investigate the nature of SO_2 binding in the absence of open metal sites, a single crystal of MFM-170· H_2O ·solv was activated under mild conditions to remove free solvent molecules whilst leaving the axial water molecule bound to the Cu centre. The resultant MFM-170· H_2O was loaded with 1 bar SO_2 and subsequent refinement of the diffraction data gave a structure with formula of $[Cu_2(L)(H_2O)_{0.79}](SO_2)_{3.27}$ (denoted MFM-170· H_2O ·3.27 SO_2). Significantly, of the six SO_2 molecules previously located in MFM-170·5.46 SO_2 , four are also present in MFM-170· H_2O ·3.27 SO_2 (Fig. S26). Clearly, the site Cu(II)-bound $SO_2(2)$ was absent in MFM-170· H_2O ·3.27 SO_2 , and as $SO_2(2)$ is a primary

site of interaction for SO₂(5), the latter was not located either. However, overall the structural analysis shows that saturation of the copper sites in MFM-170 with H₂O does not greatly reduce the SO₂ binding capacity, consistent with the retention of high uptake capacity in MFM-170·H₂O.

In situ spectroscopic analysis of host-guest binding dynamics. *In situ* FTIR spectroscopic studies were conducted for MFM-170 as a function of SO₂ loading (Fig. 6). The growth of a new peak at 1143 cm⁻¹ was assigned to the ν₁ symmetric stretch of adsorbed SO₂, which increases as a function of SO₂ partial pressure (pp). This symmetric band is red-shifted from 1152 cm⁻¹ (Δ = -9 cm⁻¹) for free SO₂, confirming its interaction with the framework. A second new band, assigned to the ν₃ asymmetric stretch of adsorbed SO₂, grows and red-shifts from 1340 cm⁻¹ at 0.01 ppSO₂ to 1320 cm⁻¹ at 0.10 ppSO₂. These bands show larger shifts compared to gas phase SO₂ (Δ = -41 cm⁻¹ at 0.10 ppSO₂), but are consistent with physisorption of SO₂.^{37,38}

Significant vibrational changes of the framework were also observed on SO₂ adsorption. The carboxylate ν_{as}(COO) mode at 1658 cm⁻¹ and ν_s(COO) mode at 1470 cm⁻¹ of MFM-170 decrease in intensity and are red-shifted to 1648 cm⁻¹ (Δ = -10 cm⁻¹) and 1462 cm⁻¹ (Δ = -8 cm⁻¹) at 0.50 ppSO₂, respectively. Interestingly, this is distinct from the blue-shifts of these bands observed in previously reported MOFs on SO₂ loading.¹⁹ This is likely due to the lack of open metal sites in those reported structures, and therefore is consistent with interactions of SO₂ with the Cu site in MFM-170. Furthermore, a red-shift (Δ = -16 cm⁻¹) of the band at 1595 cm⁻¹ on SO₂ binding, assigned to the pyridine ring vibrational band ν(CC/CN), suggests a weakening of the pyridine N-Cu coordination on SO₂ adsorption.³⁹

In situ INS experiments were conducted for dry and wet MFM-170 to gain further insight into the dynamics of SO₂ binding (Figs. 6, S24). Comparison of the spectra of bare MFM-170 and MFM-170·H₂O allows clear assignment of peaks assigned to water with a translational mode at 30 meV, rocking mode at 48 meV and wagging and twisting modes at 61 and 66 meV. The peak observed at 8.3 meV in the bare MOF can be attributed to a lattice mode which, on SO₂ loading, increases in intensity and shifts to 9.2 meV, suggesting a stiffening effect in MFM-170 on SO₂ binding. Overall, there is lack of change to the INS features upon SO₂ adsorption in MFM-170, indicating a moderate-to-weak host-guest interaction, fully consistent with the reversibility of SO₂ adsorption and full retention of the crystal structure of MFM-170 on regeneration. Upon SO₂ loading of MFM-170·H₂O, notable spectral changes are observed, attributed to interactions between bound water and SO₂ molecules. The broad translational band increases in intensity, whilst the water rocking mode increases in intensity with a blue-shift from 48 to 49 meV. The librational mode at 66 meV also blue-shifts to 67 meV with a decrease in intensity. Importantly, subsequent activation of the SO₂-adsorbed MFM-170·H₂O at 373 K under vacuum removed all peaks assigned to water, and led to a spectrum consistent with the dry bare MOF, further evidencing the stability of the MOF to humid SO₂.

Dynamic breakthrough separation of SO₂ in MFM-170. To test the effect of humidity on SO₂ adsorption in MFM-170, dynamic breakthrough experiments were conducted using gas mixtures of either 99.75% He and 2500 ppm SO₂ or 98.25 % He, 1.5 % H₂O, 2500 ppm SO₂ (Fig. 3c). Due to the experimental set-up, He was used instead of N₂ as a non-interacting component (see SI for details). Under dry conditions, SO₂ begins to breakthrough at dimensionless time τ = 420 and reaches a maximum by τ = 1400. With the

addition of 1.5% water, MFM-170 exhibits a slightly reduced SO₂ retention time at $\tau = 370$. Importantly, three cycles of SO₂ breakthrough and desorption (1 x dry cycle and 2 x wet cycles; Fig 3c) confirmed no significant deterioration in performance. To investigate further the separation ability for SO₂/CO₂, breakthrough experiments were also carried out using simulated flue gas mixtures for a fully-activated sample and a water-saturated sample of MFM-170 (81.6-84.8% He, 15-18% CO₂ and 2500-4050 ppm SO₂; Fig. 3d). For the dry sample, the breakthrough curve at 298 K shows that CO₂ is the first component eluted through the fixed-bed packed of MFM-170 and breaks through at dimensionless time $\tau = 14$. In comparison, SO₂ was selectively retained by MFM-170 and breaks through much later ($\tau \approx 350$) with maximum output observed by $\tau = 1450$. After the breakthrough of SO₂, the packed bed was regenerated at 298 K by flowing pure helium through it, and this results in rapid desorption of both CO₂ and SO₂. No more SO₂ was detected in the effluent stream when the temperature was subsequently increased to 423 K, indicating the complete desorption of SO₂ and regeneration of MFM-170 at 298 K. Crucially, the ability of MFM-170 to separate SO₂ from CO₂ in the presence of a large quantity of water was confirmed by repeating the breakthrough experiments with a water-saturated fixed-bed. The column was exposed to a stream of 3% H₂O in He until breakthrough and saturation of water was observed. The subsequent breakthrough experiment demonstrated excellent SO₂/CO₂ separation under these conditions (Fig. 3d). Interestingly, whilst the breakthrough times were slightly decreased for both components than in the above experiments, CO₂ is affected more severely with a much steeper breakthrough. Unlike the dry sample, a significant roll-up effect is observed for CO₂ under humid conditions, indicating a large displacement of weakly bound CO₂ by SO₂, likely due to the formation of H₂SO₃ complexes in the pore. This suggests that the SO₂/CO₂ separation in MFM-170 could be enhanced under humid conditions. It has been suggested that 313-333 K represents a temperature range that is suitable for purifying flue gas streams from coal-fired powerplants.^{2,3} Therefore, breakthrough experiments were also attempted for an activated packed bed of MFM-170 at elevated temperatures of 323 and 348 K (Fig. S25). Importantly, a very clear separation between CO₂ and SO₂ is evident at both temperatures, though, as expected, with reduced retention time.

Conclusions

The development of efficient strategies to fully mitigate emissions of SO₂ from combustion and to achieve efficient SO₂ storage and safe transport remains a fundamental challenge for many industries, power-plants and marine transport sectors. Although emerging MOF materials show great promise as sorbents for a wide range of inert gases, relatively little success has been achieved on the adsorptive removal of SO₂, primarily due to the generally limited reversibility and/or stability of MOFs upon contact with highly corrosive SO₂. The present work describes a high SO₂ uptake of 17.5 mmol g⁻¹ at ambient conditions in a remarkably stable MOF with open Cu(II) sites with high selectivity for SO₂ over CO₂ and N₂. The binding sites of SO₂ in MFM-170 have been elucidated using *in situ* single crystal diffraction which revealed the reversible coordination of SO₂ at open Cu(II) sites and five other binding sites at crystallographic resolution. Crucially, the open Cu(II) site has been identified as the most thermodynamically favoured binding site for SO₂. In addition to static crystallography studies, dynamic

vibrational modes were investigated using INS and FT-IR microscopy as a function of SO₂ loading. The industrial promise of MFM-170 has been demonstrated through dynamic breakthrough experiments which showed efficient separation of SO₂ from simulated flue gas mixtures, even in the presence of water and at elevated temperatures.

References.

1. Rezaei, F. *et al.* SO_x/NO_x Removal from flue gas streams by solid adsorbents: a review of current challenges and future directions. *Energy & Fuels* **29**, 5467–5486 (2015).
2. Gao, J. *et al.* Pilot-scale experimental study on the CO₂ capture process with existing of SO₂: degradation, reaction rate, and mass transfer. *Energy & Fuels* **25**, 5802–5809 (2011).
3. Ding, S. *et al.* Significant promotion effect of Mo additive on a novel Ce–Zr mixed oxide catalyst for the selective catalytic reduction of NO_x with NH₃. *ACS Appl. Mater. Interfaces* **7**, 9497–9506 (2015).
4. Kinnunen, N. M. *et al.* Case study of a modern lean-burn methane combustion catalyst for automotive applications: What are the deactivation and regeneration mechanisms? *Appl. Catal. B Environ.* **207**, 114–119 (2017).
5. Han, X., Yang, S., Schröder, M. Porous metal–organic frameworks as emerging sorbents for clean air. *Nat. Rev. Chem.*, **3**, 108–118 (2019).
6. Raymundo-Piñero, E. *et al.* Factors controlling the SO₂ removal by porous carbons: relevance of the SO₂ oxidation step. *Carbon*, **38**, 335–344 (2000).
7. Mathieu, Y. *et al.* Adsorption of SO_x by oxide materials: A review. *Fuel Process. Technol.* **114**, 81–100 (2013).
8. Kohl, A. L. & Nielsen, R. *Gas Purification*. (Gulf Professional Publishing, 1997).
9. Nabais, A. R. *et al.* CO₂/N₂ gas separation using Fe(BTC)-based mixed matrix membranes: a view on the adsorptive and filler properties of metal-organic frameworks. *Sep. Purif. Technol.* **202**, 174–184 (2018).
10. Peng, J. *et al.* Efficient kinetic separation of propene and propane using two microporous metal organic frameworks. *Chem. Commun.* **53**, 9332–9335 (2017).
11. Chen, D.-M. *et al.* Tunable robust pacs-MOFs: a platform for systematic enhancement of the C₂H₂ uptake and C₂H₂/C₂H₄ separation performance. *Inorg. Chem.* **57**, 2883–2889 (2018).
12. Zhong, R. *et al.* A solvent ‘squeezing’ strategy to graft ethylenediamine on Cu₃(BTC)₂ for highly efficient CO₂/CO separation. *Chem. Eng. Sci.* **184**, 85–92 (2018).
13. Zhang, Z. *et al.* MOFs for CO₂ capture and separation from flue gas mixtures: the effect of multifunctional sites on their adsorption capacity and selectivity. *Chem. Commun.* **49**, 653–661 (2013).
14. Peralta, D. *et al.* Comparison of the behavior of metal–organic frameworks and zeolites for hydrocarbon separations. *J. Am. Chem. Soc.* **134**, 8115–8126 (2012).
15. Carter, J. H. *et al.* Exceptional adsorption and binding of sulfur dioxide in a robust zirconium-based metal–organic framework. *J. Am. Chem. Soc.* **140**, 15564–15567 (2018).
16. Cui, X. *et al.* Ultrahigh and selective SO₂ uptake in inorganic anion-pillared hybrid porous materials. *Adv. Mater.* **29**, 1606929 (2017).
17. Glomb, S. *et al.* Metal–organic frameworks with internal urea-functionalized dicarboxylate linkers for SO₂ and NH₃ adsorption. *ACS Appl. Mater. Interfaces* **9**, 37419–37434 (2017).

18. Yang, S. *et al.* Irreversible network transformation in a dynamic porous host catalyzed by sulfur dioxide. *J. Am. Chem. Soc.* **135**, 4954–4957 (2013).
19. Tan, K. *et al.* Mechanism of preferential adsorption of SO₂ into two microporous paddle wheel frameworks M(bdc)(ted)_{0.5}. *Chem. Mater.* **25**, 4653–4662 (2013).
20. Savage, M. *et al.* Selective adsorption of sulfur dioxide in a robust metal-organic framework material. *Adv. Mater.* **28**, 8705–8711 (2016).
21. Li, L. *et al.* Post-synthetic modulation of the charge distribution in a metal–organic framework for optimal binding of carbon dioxide and sulfur dioxide. *Chem. Sci.* **10**, 1472–1482 (2019).
22. Lee, G.-Y. *et al.* Amine-functionalized covalent organic framework for efficient SO₂ capture with high reversibility. *Sci. Rep.* **7**, 557 (2017).
23. Thallapally, P. K. *et al.* Prussian blue analogues for CO₂ and SO₂ capture and separation applications. *Inorg. Chem.* **49**, 4909–4915 (2010).
24. Fernandez, C. *et al.* Gas-induced expansion and contraction of a fluorinated metal–organic framework. *Cryst. Growth Des.* **10**, 1037–1039 (2010).
25. Tchalala, M. R. *et al.* Fluorinated MOF platform for selective removal and sensing of SO₂ from flue gas and air. *Nat. Commun.* **10**, 1328 (2019).
26. Riboldi, L. & Bolland, O. Overview on pressure swing adsorption (PSA) as CO₂ capture technology: state-of-the-art, limits and potentials. *Energy Procedia* **114**, 2390–2400 (2017).
27. Riboldi, L. & Bolland, O. Evaluating pressure swing adsorption as a CO₂ separation technique in coal-fired power plants. *Int. J. Greenh. Gas Control* **39**, 1–16 (2015).
28. Britt, D. *et al.* Highly efficient separation of carbon dioxide by a metal-organic framework replete with open metal sites. *Proc. Natl. Acad. Sci.* **106**, 20637–20640 (2009).
29. Wong-Foy, A. G., Matzger, A. J. & Yaghi, O. M. Exceptional H₂ saturation uptake in microporous metal–organic frameworks. *J. Am. Chem. Soc.* **128**, 3494–3495 (2006).
30. Caskey, S. R., Wong-Foy, A. G. & Matzger, A. J. Dramatic tuning of carbon dioxide uptake via metal substitution in a coordination polymer with cylindrical pores. *J. Am. Chem. Soc.* **130**, 10870–10871 (2008).
31. Britt, D., Tranchemontagne, D. & Yaghi, O. M. Metal-organic frameworks with high capacity and selectivity for harmful gases. *Proc. Natl. Acad. Sci.* **105**, 11623–11627 (2008).
32. Guillerm, V. *et al.* A supermolecular building approach for the design and construction of metal–organic frameworks. *Chem. Soc. Rev.* **43**, 6141–6172 (2014).
33. Park, J. *et al.* A versatile metal–organic framework for carbon dioxide capture and cooperative catalysis. *Chem. Commun.* **48**, 9995 (2012).
34. Lu, Z. *et al.* The utilization of amide groups to expand and functionalize metal-organic frameworks simultaneously. *Chem. - A Eur. J.* **22**, 6277–6285 (2016).
35. Branton, P. J., Hall, P. G., Treguer, M. & Sing, K. S. W. Adsorption of carbon dioxide, sulfur dioxide and water vapour by MCM-41, a model mesoporous adsorbent. *J. Chem. Soc., Faraday Trans.* **91**, 2041–2043 (1995).
36. Goodman, A. L., Li, P., Usher, C. R. & Grassian, V. H. Heterogeneous uptake of sulfur dioxide on aluminum and magnesium oxide particles. *J. Phys. Chem. A* **105**, 6109–6120 (2001).
37. Tan, K. *et al.* Interaction of acid gases SO₂ and NO₂ with coordinatively unsaturated metal organic frameworks: MOF-74 (M = Zn, Mg, Ni, Co). *Chem. Mater.* **29**, 4227–4235 (2017).
38. Schneider, W. F., Li, J. & Hass, K. C. Combined computational and experimental investigation of SO_x adsorption on MgO. *J. Phys. Chem. B* **105**, 6972–6979 (2001).

39. Marinho, M. V. *et al.* Synthesis, crystal structure, and spectroscopic characterization of trans-bis[(μ -1,3-bis(4-pyridyl)propane)(μ -(3-thiopheneacetate-*O*))(3-thiopheneacetate-*O*)]dicopper(II), $\{[\text{Cu}_2(\text{O}_2\text{CCH}_2\text{C}_4\text{H}_3\text{S})_4 \mu\text{-}(\text{BPP})_2]\}_n$: from a dinuclear paddle-wheel copper(II) unit to a 2-D coordination polymer involving monatomic carboxylate bridges. *Inorg. Chem.* **43**, 1539–1544 (2004).

Methods

SO₂ safety: All systems involved in the supply, delivery and measurement of SO₂ were rigorously leak tested and used only within range of a SO₂ detection system with a sensitivity of 0.1 ppm. All gases exhausted from experimental apparatus were diluted with a flow of N₂ and fed into fume hood extracts.

Synthesis of MFM-170·solv: $[\text{Cu}_2(\text{C}_{33}\text{H}_{17}\text{NO}_8)(\text{H}_2\text{O})] \cdot 6(\text{C}_3\text{H}_7\text{NO})$: H₄L (192 mg, 0.36 mmol) and $\text{Cu}(\text{NO}_3)_2 \cdot 2.5\text{H}_2\text{O}$ (298 mg, 1.28 mmol) were dissolved in a solution of DMF:H₂O (48 mL, 5:1) and acidified with conc. HNO₃ (0.3 mL). The solution was heated in a Schott bottle at 80°C for 18 h until blue octahedral crystals precipitated. The product was filtered, washed with hot DMF and dried in air (320 mg, 86%). IR (ATR) cm⁻¹: 3382 (b), 1698 (w), 1645 (s), 1598 (s), 1557 (s), 1428 (s), 1378 (vs), 1298 (s), 1244 (w), 1170 (w), 1116 (m). Elemental analysis (% calculated/found): C 53.46/52.93; H 4.89/4.61; N 6.93/7.18. Powder samples of MFM-170·H₂O·solv in this work were obtained by stirring identical reaction mixtures in an open round bottom flask. Whilst the sum formula from single crystal X-ray diffraction included in the refinement model is $\text{Cu}_2(\text{C}_{33}\text{H}_{17}\text{NO}_8)(\text{H}_2\text{O})_{0.65}$, the final formula of $[\text{Cu}_2(\text{C}_{33}\text{H}_{17}\text{NO}_8)(\text{H}_2\text{O})] \cdot 6(\text{C}_3\text{H}_7\text{NO})$ was calculated from a combination of TGA and elemental analysis, accounting for disordered solvent molecules.

Gas Cell Details and Structure Determination and Refinement of MFM-170·H₂O·solv, MFM-170, MFM-170·5.46SO₂, MFM-170·0.09SO₂, MFM-170·H₂O and MFM-170·H₂O·3.27SO₂

Gas-loaded single crystal X-ray diffraction experiments of MFM-170 were carried out at beamline 11.3.1 of the Advanced Light Source, Berkeley. Single crystals of MFM-170 were placed in a capillary gas handling cell and were evacuated *in situ* under a hot stream of N₂ centred on the capillary. The activated crystals were then cooled to *ca.* 300 K before being dosed with 1 bar of SO₂. The locations of the SO₂ molecules could be discerned from the Fourier difference maps at 300 K (MFM-170·5.46SO₂, MFM-170·0.09SO₂) and 260 K (MFM-170·H₂O·3.27SO₂) and were included in the refinement model with bond distances and angles constrained to ideal values. See Supplementary Information for details of structure determination and refinement.

Crystal Data for MFM-170·H₂O·solv $[\text{Cu}_2(\text{C}_{33}\text{H}_{17}\text{NO}_8)(\text{H}_2\text{O})_{0.65}]$; blue octahedron (0.1 x 0.1 x 0.1 mm). Cubic, *Im-3m*, $a = 33.5294(17) \text{ \AA}$, $V = 37963(7) \text{ \AA}^3$, $Z = 24$, $\rho_{\text{calcd}} = 0.729 \text{ g cm}^{-3}$, $\mu_{\text{calcd}} = 0.883 \text{ mm}^{-1}$, $F(000) = 8413$. A total of 45304 reflections were collected, of which 1475 were unique giving $R_{\text{int}} = 0.153$. Final $R_1 (wR_2) = 0.0465 (0.1226)$ with $\text{GoF} = 1.130$. The final difference Fourier extreme were 0.427 and $-0.568 \text{ e \AA}^{-3}$.

Crystal Data for desolvated MFM-170 $[\text{Cu}_2(\text{C}_{33}\text{H}_{17}\text{NO}_8)]$; purple octahedron (0.1 x 0.1 x 0.1 mm). Cubic, *Im-3m*, $a = 33.609(2) \text{ \AA}$, $V = 37694(6) \text{ \AA}^3$, $Z = 24$, $\rho_{\text{calcd}} = 0.722 \text{ g cm}^{-3}$, $\mu_{\text{calcd}} = 0.883 \text{ mm}^{-1}$, $F(000) = 8256$. A total of 42452 reflections were collected, of which 1043 were unique giving $R_{\text{int}} = 0.197$. Final $R_1 (wR_2) = 0.039 (0.097)$ with $\text{GoF} = 1.045$. The final difference Fourier extreme were 0.320 and $-0.381 \text{ e \AA}^{-3}$.

Crystal Data for MFM-170·5.46SO₂ $[\text{Cu}_2(\text{C}_{33}\text{H}_{17}\text{NO}_8)(\text{SO}_2)_{0.67}](\text{SO}_2)_{4.79}$; blue octahedron (0.1 x 0.1 x 0.1 mm). Cubic, *Im-3m*, $a = 33.5808(17) \text{ \AA}$, $V = 37868(6) \text{ \AA}^3$, $Z = 24$, $\rho_{\text{calcd}} = 1.086 \text{ g cm}^{-3}$, $\mu_{\text{calcd}} = 1.144 \text{ mm}^{-1}$, $F(000) = 12448$.

A total of 105823 reflections were collected, of which 2202 were unique giving $R_{\text{int}} = 0.186$. Final $R_1 (wR_2) = 0.117 (0.331)$ with $\text{GoF} = 1.663$. The final difference Fourier extreme were 1.577 and $-1.156 \text{ e}\text{\AA}^{-3}$.

Crystal Data for MFM-170-0.09SO₂ [$\text{Cu}_2(\text{C}_{33}\text{H}_{17}\text{NO}_8)(\text{SO}_2)_{0.09}$]; blue octahedron (0.1 x 0.1 x 0.1 mm). Cubic, $Im\bar{3}m$, $a = 33.5458(19) \text{ \AA}$, $V = 37750(6) \text{ \AA}^3$, $Z = 24$, $\rho_{\text{calcd}} = 0.727 \text{ g cm}^{-3}$, $\mu_{\text{calcd}} = 0.890 \text{ mm}^{-1}$, $F(000) = 8324$. A total of 73416 reflections were collected, of which 1471 were unique giving $R_{\text{int}} = 0.173$. Final $R_1 (wR_2) = 0.0411 (0.092)$ with $\text{GoF} = 1.083$. The final difference Fourier extreme were 0.517 and $-0.474 \text{ e}\text{\AA}^{-3}$.

Crystal Data for MFM-170-H₂O [$\text{Cu}_2(\text{C}_{33}\text{H}_{17}\text{NO}_8)(\text{H}_2\text{O})_{0.50}$]; blue octahedron (0.1 x 0.1 x 0.1 mm). Cubic, $Im\bar{3}m$, $a = 33.4562(16) \text{ \AA}$, $V = 37448(5) \text{ \AA}^3$, $Z = 24$, $\rho_{\text{calcd}} = 0.736 \text{ g cm}^{-3}$, $\mu_{\text{calcd}} = 0.895 \text{ mm}^{-1}$, $F(000) = 8376$. A total of 110623 reflections were collected, of which 2211 were unique giving $R_{\text{int}} = 0.0699$. Final $R_1 (wR_2) = 0.0565 (0.1799)$ with $\text{GoF} = 1.124$. The final difference Fourier extreme were 0.702 and $-0.458 \text{ e}\text{\AA}^{-3}$.

Crystal Data for MFM-170-H₂O-3.27SO₂ [$\text{Cu}_2(\text{C}_{33}\text{H}_{17}\text{NO}_8)(\text{H}_2\text{O})_{0.79}(\text{SO}_2)_{3.27}$]; blue octahedron (0.1 x 0.1 x 0.1 mm). Cubic, $Im\bar{3}m$, $a = 33.610(4) \text{ \AA}$, $V = 37968(12) \text{ \AA}^3$, $Z = 24$, $\rho_{\text{calcd}} = 0.951 \text{ g cm}^{-3}$, $\mu_{\text{calcd}} = 1.039 \text{ mm}^{-1}$, $F(000) = 10957$. A total of 84668 reflections were collected, of which 1720 were unique giving $R_{\text{int}} = 0.078$. Final $R_1 (wR_2) = 0.0947 (0.3006)$ with $\text{GoF} = 1.529$. The final difference Fourier extreme were 0.909 and $-0.618 \text{ e}\text{\AA}^{-3}$.

A more detailed description of single crystal X-ray diffraction data can be found in the supplementary information.

Gas adsorption isotherms and breakthrough experiment: Measurements of SO₂ adsorption isotherms (0–1 bar) were performed using a Xemis gravimetric adsorption apparatus (Hiden Isochema, Warrington, UK) equipped with a clean ultrahigh vacuum system. The pressure in the system is accurately regulated by mass flow controllers. Research grade SO₂ and He were purchased from AIRLIQUIDE or BOC and used as received. In a typical gas adsorption experiment, 70-100 mg of MFM-170-H₂O-solv was loaded into the Xemis, and degassed at 423 K and high dynamic vacuum (10^{-10} bar) for 1 day to give desolvated MFM-170.

Breakthrough experiments were carried out in a 7 mm diameter fixed-bed tube of 120 mm length packed with 1.5 g of MFM-170 powder (particle size < 5 microns). The total volume of the bed was *ca.* 5 cm³. The sample was heated at 423 K under a flow of He for 2 days for complete activation. The fixed-bed was then cooled to room temperature (298 K) using a temperature programmed water bath and the breakthrough experiment was performed with streams of SO₂ (0.5% diluted in He) and CO₂ at atmospheric pressure and room temperature. The flow rate of the entering gas mixture was maintained at 47 mL min⁻¹, and the gas concentration, C , of SO₂ and CO₂ at the outlet determined by mass spectrometry and compared with the corresponding inlet concentration C_0 , where $C/C_0 = 1$ indicates complete breakthrough. A more detailed description is given in SI.

Supplementary Information is available in the online version of the paper.

Acknowledgements. We thank EPSRC (EP/I011870), ERC (AdG 742041), the Royal Society and University of Manchester for funding. We are especially grateful to Diamond Light Source (DLS), Advanced Light Source, Oak Ridge National Laboratory and STFC/ISIS Neutron Facility for access to the Beamlines B22/I11, 11.3.1, VISION and TOSCA, respectively. We thank Mark Kibble for the help at TOSCA beamline. The computing resources were made available through the VirtuES and the ICE-MAN projects, funded by Laboratory Directed Research and Development program at ORNL. This research used

resources of the Advanced Light Source, which is a DOE Office of Science User Facility under contract no. DE-AC02-05CH11231. JL, XZ thank China Scholarship Council for funding.

Author Contributions. GLS, JEE: synthesis and characterisation of MOF samples, measurements of adsorption isotherms. GLS, XH: measurements and analysis of the breakthrough data. GLS, XZ, SPA, LJM, SJTL, SY: collection and analysis of synchrotron single crystal X-ray diffraction data. GLS, HGWG, YC, SR, AJRC: collection and analysis of neutron scattering data. GLS, SJD and CCT: collection and analysis of long duration synchrotron X-ray diffraction data. GLS, JL, NMJ, MDF, GC, TLE: collection and analysis of synchrotron IR data. SY and MS: overall design and direction of project. GLS, SY and MS: preparation of the manuscript with help from all authors.

Author Information. The crystal structures are available free of charge from the Cambridge Crystallographic Data Centre under reference number CCDC-1538125-6, 1538129, 1853512-4. Reprints and permissions information is available at www.nature.com/reprints. The authors declare no competing financial interests. Correspondence and requests for materials should be addressed to S.Y. (Sihai.Yang@manchester.ac.uk) and M.S. (M.Schroder@manchester.ac.uk).

Competing financial interests. The authors declare no competing financial interests.

Data availability. All relevant data are available from the authors, and/or are included with the manuscript.

Figures and Tables

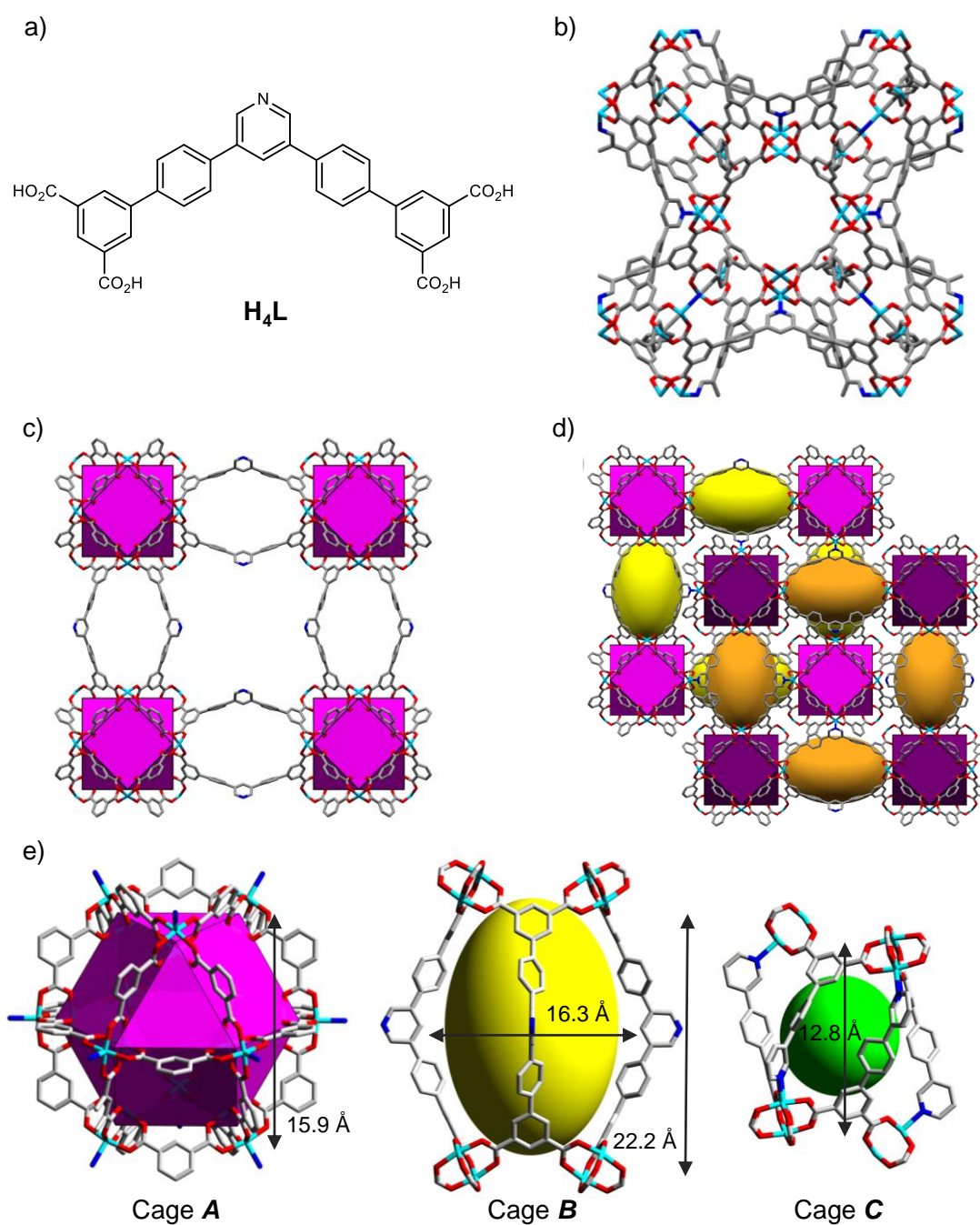


Fig. 1: Structure of MFM-170 solved from single crystal X-ray data. Views of a) structure of H₄L; b) the unit cell of MFM-170; c) the simplified structure showing the ‘smaller’ net of MFM-170; d) full structure resulting from connection of the two smaller nets; e) metal-ligand Cages A, B and C, observed in MFM-170.

Table 1: Comparison of data for SO₂ adsorbents.

Material	BET Surface Area (m ² g ⁻¹)	Open Metal Site	1 Bar SO ₂ Uptake at 298 K (mmol g ⁻¹)	Ref
MFM-170	2,408	Y	17.5	This work
MFM-170-H ₂ O	2,003	N	13.0	This work
MFM-601	3644	N	12.3	15
SIFSIX-1-Cu	1,337	N	11.0	16
[Zn ₂ (L ₁) ₂ (bipy)]	275 ^a	N	10.9 ^b	17
MFM-202a	2,220	N	10.2 ^c	18
Ni(bdc)(ted) _{0.5}	1,783	N	10.0	19
Mg-MOF-74	1,475	Y	8.6	19
MFM-300(In)	1,071	N	8.3	20
MFM-305	799	N	7.0	21
SIFSIX-2-Cu-i	735	N	6.9	16
PI-COF-m	1,003	n/a	6.5	22
SIFSIX-2-Cu	3,140	N	6.5	16
[Zn ₂ (L ₁) ₂ (bpe)]	379 ^a	N	6.4 ^b	17
PI-COF-m10	831	n/a	6.3	22
PI-COF-m20	548	n/a	5.6	22
PI-COF-m40	279	n/a	5.5	22
MFM-305-CH ₃	256	N	5.2	21
MFM-600	2281	N	5.0	15
PI-COF-m60	93	n/a	4.7	22
Zn(bdc)(ted) _{0.5}	1,888	N	4.4	19
KAUST-8	250	Y	~2.9 ^d	25
SIFSIX-3-Ni	223	N	2.7	16
KAUST-7	280	N	~2.6 ^d	25
Prussian Blue (CoCo)	712	N	2.5	23
[Zn ₄ (μ ₄ -O)(L ₁) ₃]	299 ^a	N	2.2 ^b	17
FMOF-2	378	Y	2.2	24
SIFSIX-3-Zn	250	N	2.1	16

^a DFT-calculated surface area ^b 293K. ^c MFM-202a exhibits reversible SO₂ adsorption at 273-303K, but undergoes an irreversible phase change at lower temperatures. ^d estimated from isotherm

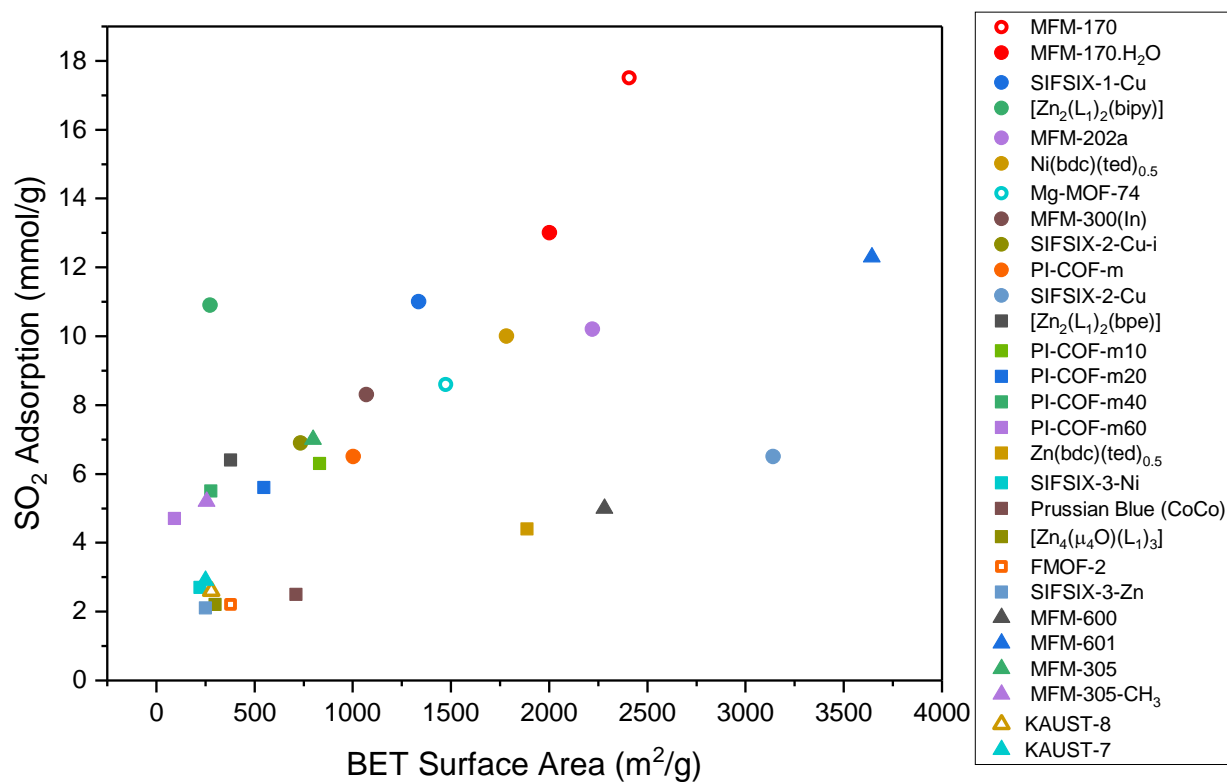


Fig. 2: Comparison of SO₂ uptakes of reported MOFs and COFs at 1.0 bar and 298 K. Plot of SO₂ adsorption (1.0 bar, 298 K) against BET surface area. Open symbols denote the presence of open metal sites in the MOF structure.

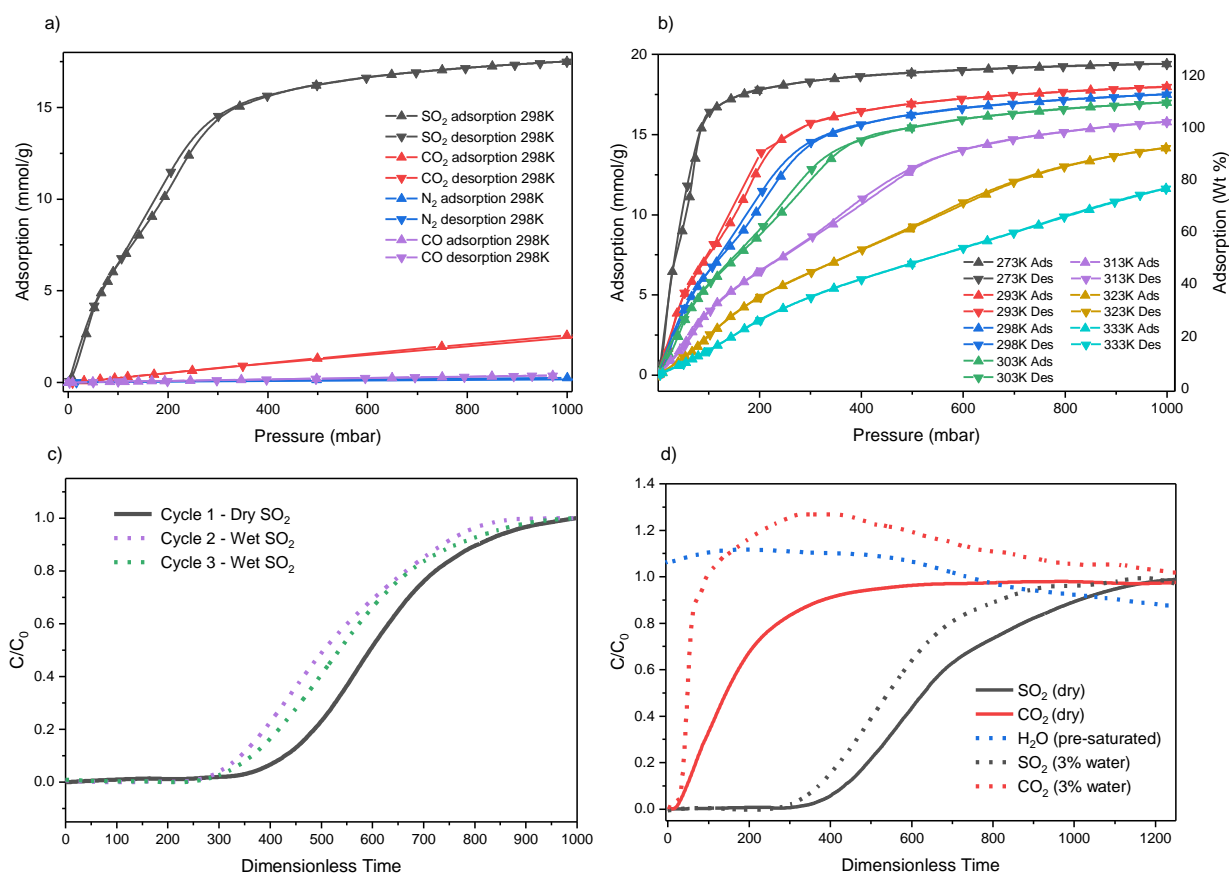


Fig. 3: Gas sorption properties of MFM-170. a) adsorption and desorption isotherms for MFM-170 at 298 K up to 1 bar for SO₂ (black), CO₂ (red), N₂ (blue) and CO (purple); b) SO₂ adsorption and desorption isotherms for MFM-170 at 273-333 K up to 1 bar. Wt % is in terms of SO₂(g)/MOF(g). c) Breakthrough curves for SO₂ at 298 K under dry (solid line) and humid (dashed lines) conditions. The consistency in the retention time for SO₂ under humid conditions confirms the high stability of MFM-170. Dry conditions: 99.75% He, 2500 ppm SO₂; Wet Conditions: 98.25% He, 1.5% H₂O, 2500 ppm SO₂. Flow rate 26 mL min⁻¹. d) Comparison of the binary SO₂/CO₂ dynamic separations at 298 K under dry (solid line) and humid (dashed line) conditions. The dry sample was first activated under a flow of He at 423 K and the subsequent gas mixture composition was 84.75% He, 15% CO₂ and 2500 ppm SO₂ at a total flow rate of 26 mL min⁻¹. For experiments under humid conditions, the bed was first exposed to a flow of 3% H₂O in He until breakthrough of water (not shown). The subsequent gas mixture composition was ~81.6% He, 18% CO₂ and 4050 ppm SO₂ with a total flow rate of 16 mL min⁻¹. Dimensionless time, τ , is equal to $t u / \epsilon L$, where t is the actual breakthrough time, u is the gas velocity, ϵ is the fractional porosity and L is the length of the fixed bed. See Supplementary Information for details.

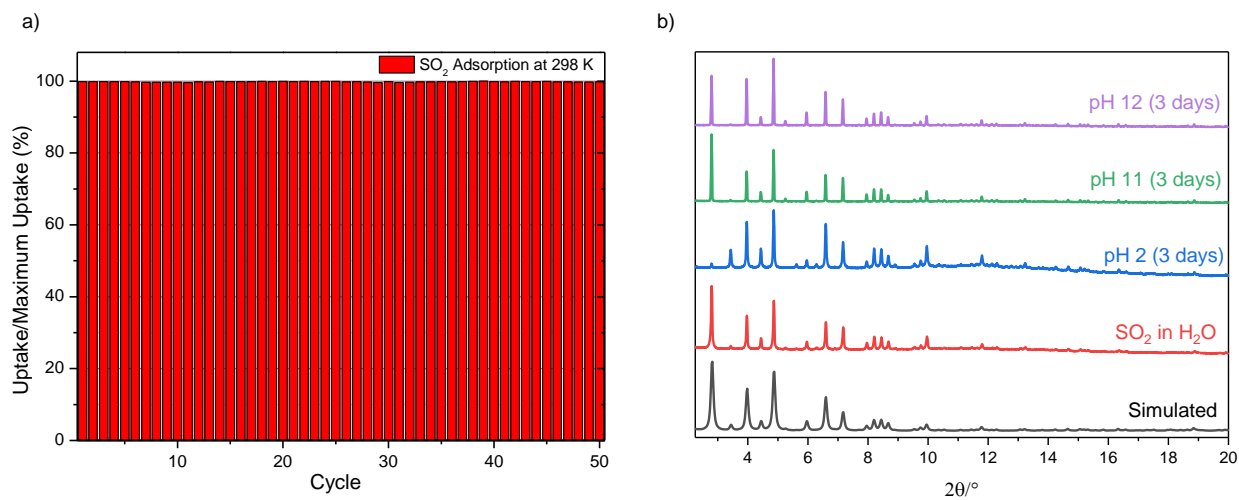


Fig. 4. Chemical stability tests for MFM-170. a) 50 adsorption-desorption cycles for SO₂ in MFM-170 at 298 K. No loss of uptake capacity is observed. b) PXR D analysis of MFM-170 exposed to various external conditions. Changes of intensities of Bragg peaks correspond to the inclusion of guest species in the pores of MFM-170. Pawley refinements are shown in the Supplementary Information.

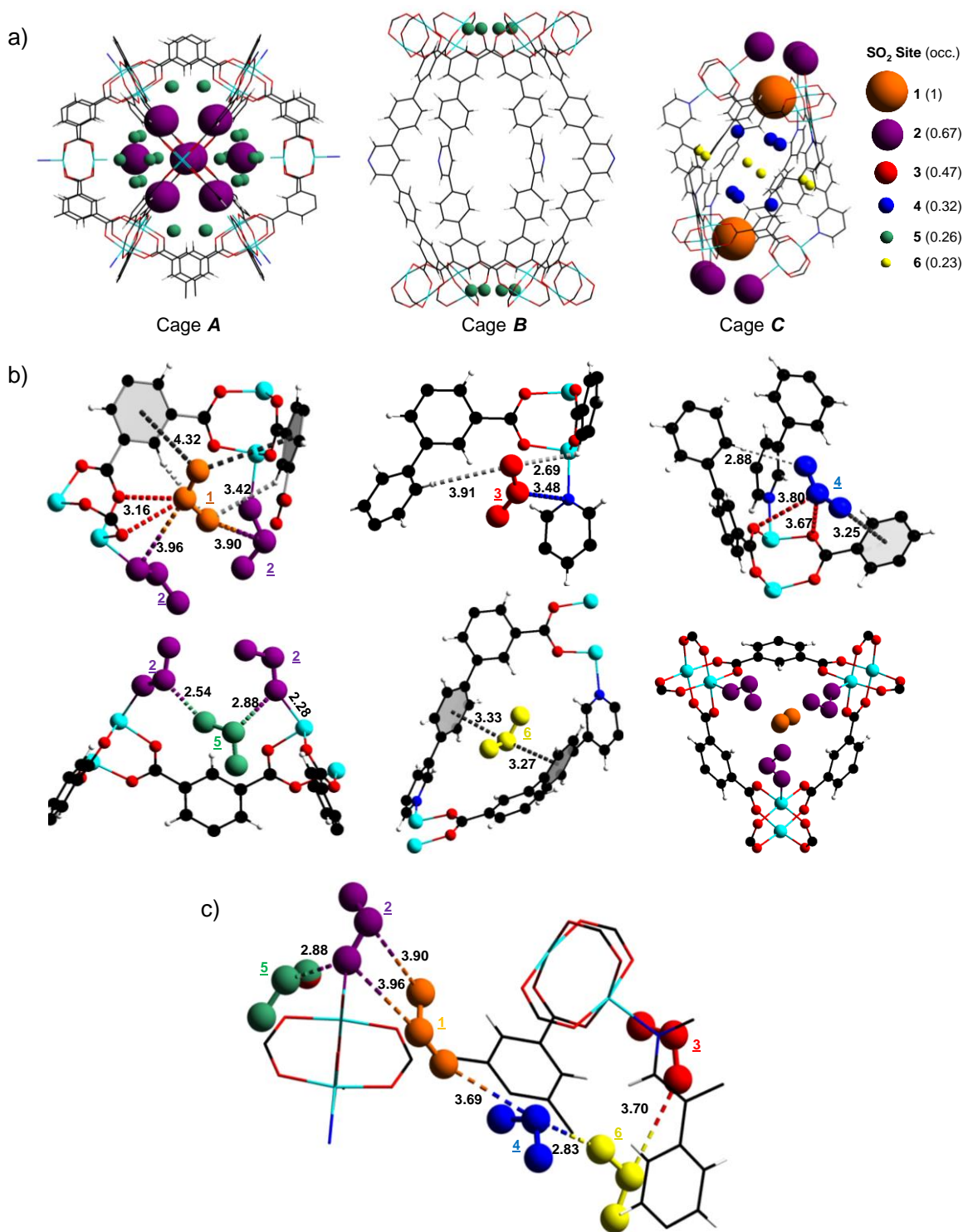


Fig. 5: Positions of SO₂ molecules located within the pores of MFM-170-5.46SO₂ from *in situ* single crystal XRD. a) Packing of SO₂ with in cages A, B and C. No ordered SO₂ was found in cage B. Size of the coloured balls depicting sites 1-6 are proportional to their occupancy. Site 3 is found in a crevice between two perpendicular cage B and are therefore not shown in the cages. b) Site (colour, occupancy): 1 (orange, 1.00); 2 (purple, 0.670); 3 (red, 0.468); 4 (blue 0.316); 5 (green, 0.262); and 6 (yellow, 0.233). c) Intermolecular interactions between adsorbed SO₂ molecules. SO₂ molecules have been magnified slightly for clarity. Distances are in Å.

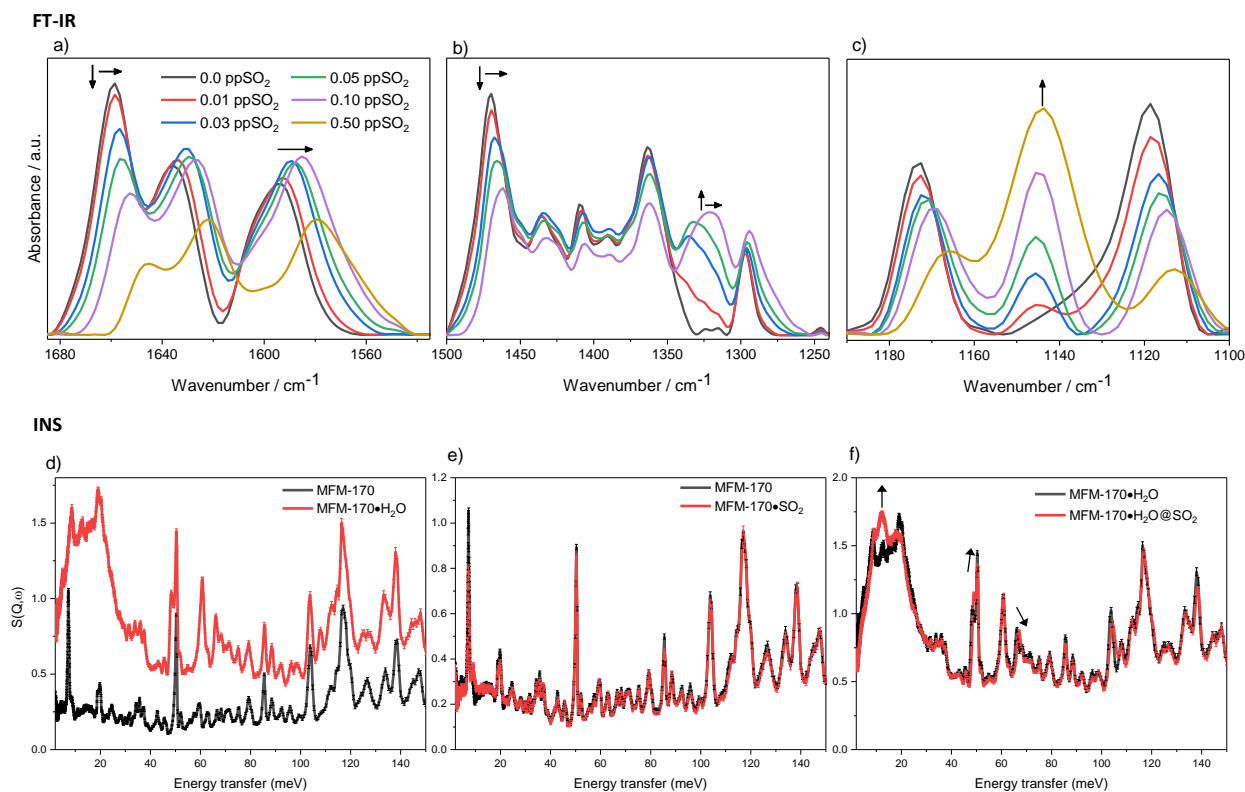


Fig 6. *In situ* vibrational spectra of MFM-170. a-c) FT-IR spectra of MFM-170 at various SO₂ loadings up to 0.50 ppSO₂. a) Redshift of carboxylate $\nu_{\text{as}}(\text{COO})$ stretching mode at 1658 cm⁻¹ and pyridine ring vibrational band $\nu(\text{CC/CN})$ at 1595 cm⁻¹; b) Red shift of $\nu_{\text{s}}(\text{COO})$ stretching mode at 1470 cm⁻¹ and the ν_3 asymmetric stretch of adsorbed SO₂; c) growth of a new band at 1143 cm⁻¹ assigned to the ν_1 symmetric stretch of adsorbed SO₂. All FT-IR spectra were collected at 1.0 bar, using N₂ as a balancing gas. The fundamental ν_3 antisymmetric stretch of gas phase SO₂ at 1361 cm⁻¹ saturates at low partial pressures in this experiment, and therefore the region of 1400-1300 cm⁻¹ was only monitored up to 0.10 ppSO₂; d-f) INS spectra of MFM-170: d) Activated MFM-170 and MFM-170·H₂O. Additional peaks in MFM-170·H₂O are attributed to vibrational modes of water molecules; e) Activated MFM-170 and MFM-170@SO₂. Minimal difference is observed between the two spectra; f) MFM-170·H₂O and MFM-170·H₂O@SO₂. Shifts in water modes are observed indicating H₂O···SO₂ interactions.